

# Effect of Axial Ligands on Photocatalytic CO<sub>2</sub> Reduction of Zirconium-Based Porphyrins

Chenyue Yong, Chi Song, Guanhong Lu, Xiao Wang, Guanqing Song, Gansheng Shi, Yan Wang, Xiaofeng Xie, and Jing Sun\*



Cite This: *ACS Appl. Energy Mater.* 2025, 8, 4379–4386



Read Online

ACCESS |



Metrics & More



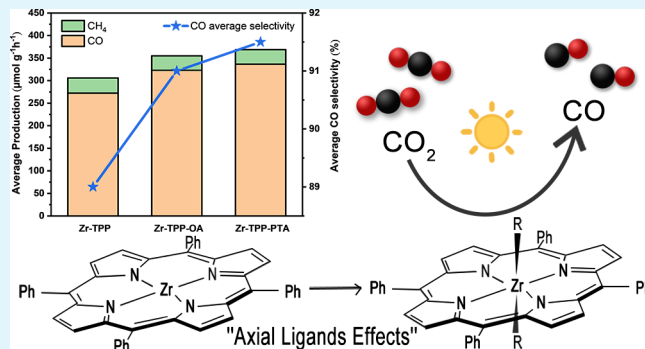
Article Recommendations



Supporting Information

**ABSTRACT:** Metalloporphyrins, with their unique large conjugated planar structure, have attracted research attention in catalysis, energy, and biomedicine. However, studies of examining the effects of axial ligands on metal centers are limited. Herein, we introduced oxalic acid and p-phthalic acid (PTA) as axial ligands into tetraphenylporphyrin zirconium (Zr-TPP). Through structural modulation of axial ligands, the zirconium-based porphyrins effectively enhance the separation and transport of photogenerated carriers and also induce an increase in charge density at the metal center atoms. These modified structures efficiently enhanced their photocatalytic performance, achieving over 90% selectivity for CO<sub>2</sub>-to-CO conversion. Specifically, the CO production with Zr-TPP is 272.43  $\mu\text{mol g}^{-1} \text{h}^{-1}$ , and it surpasses 336.5  $\mu\text{mol g}^{-1} \text{h}^{-1}$  with Zr-TPP-PTA. The photocatalytic mechanism responsible for reducing CO<sub>2</sub> to CO is explored through density functional theory calculations. This work explores axial ligand–metal interactions in porphyrin complexes, revealing that different axial ligands can affect the electronic structure of materials and improve their photocatalytic performance, providing ideas for the regulation of metalloporphyrin-based photocatalysts.

**KEYWORDS:** zirconium porphyrins, axial ligand, photocatalyst, CO<sub>2</sub> photoreduction, CO production



## 1. INTRODUCTION

The rapidly increased global greenhouse gas emissions have led to serious energy crises and climate change issues over the past few decades.<sup>1–3</sup> Photocatalytic carbon dioxide (CO<sub>2</sub>) reduction into high-value C1 chemicals provides a promising approach for mitigating these challenges by directly capturing and converting excess CO<sub>2</sub> emissions driven by sunlight.<sup>4</sup> Among various CO<sub>2</sub> reduction products, carbon monoxide (CO) has attracted significant attention due to the relatively lower thermodynamic barrier compared to the other C1 products, such as methane (CH<sub>4</sub>).<sup>5,6</sup> Nevertheless, the inert nature of the CO<sub>2</sub> molecule (the dissociation energy of the C=O bond is 806 kJ mol<sup>-1</sup>) significantly blocks the activation and subsequent reduction at catalytic sites.<sup>7</sup> The complex multielectron processes in the reaction seriously hinder the selectivity of CO conversion.<sup>8</sup> Therefore, designing and developing highly active and selective photocatalysts for CO<sub>2</sub>-to-CO conversion while deepening the understanding of the catalytic reaction mechanism are of great significance but have challenges.

Metalloporphyrins, which generally possess broad optical absorption properties and exposed metal centers as active sites for surface reactions, have emerged as promising candidates for photocatalytic CO<sub>2</sub> reduction.<sup>9–12</sup> However, due to the rapid

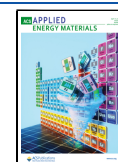
recombination of photogenerated electron–hole pairs and the complex surface reduction reactions, there is still a long way to go to achieve large-scale photocatalytic CO<sub>2</sub>-to-CO conversion. Recent research have suggested that the introduction of additional axial ligands can significantly influence the electronic properties of the metal unit via a “push effect.”<sup>13,14</sup> For instance, Qian et al.<sup>15</sup> designed a ferrocene-based tin(IV) porphyrin axially coordinated with fullerene (C<sub>60</sub>) to generate a long-lived charge separation and sluggish charge recombination. Similarly, Zheng et al.<sup>16</sup> regulate an electrochemical reduction of CO<sub>2</sub> through introducing thiocyanate as an axial ligand into iron(III) tetraphenyl porphyrin via a counter anion exchanging reaction. Despite these advances, the impact of axial ligand incorporation into metalloporphyrins on their photocatalytic properties remains poorly understood, which limits the progress in elucidating the interactions between ligands and metal centers at the molecular level.

**Received:** December 22, 2024

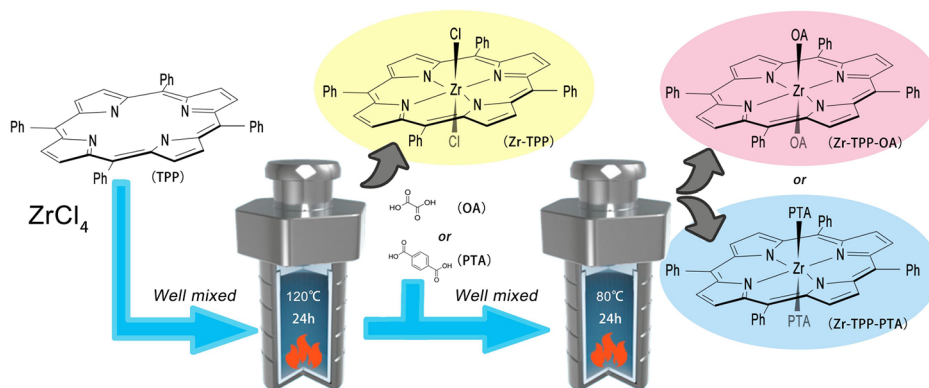
**Revised:** March 23, 2025

**Accepted:** March 27, 2025

**Published:** April 2, 2025



Scheme 1. Schematic Diagram of the Synthesis Process of Zr Porphyrin Coordination Compounds



Herein, we report the rational design and synthesis of a series of Zr (IV) meso-tetraphenyl porphyrin (Zr-TPP)-based photocatalysts functionalized with axial ligands, specifically oxalic acid (Zr-TPP-OA) and p-phthalic acid (Zr-TPP-PTA), through the coordination interactions between the Zr metal center and the dicarboxylic acid molecules. Furthermore, the structural and performance relationships between the axial ligands and the Zr metal center were comprehensively investigated. The introduction of axial ligands optimized the local electronic structure of the Zr metal center and facilitated the separation and transport of photogenerated carriers. Meanwhile, the axial ligand effectively increases the electron density of the Zr metal center, which is conducive to improving the adsorption and activation of CO<sub>2</sub> molecules at the Zr center through the “push effect”, emphasizing the key role of the axial ligand in improving the overall photocatalytic performance.<sup>17,18</sup> Systematic experiments and theoretical calculations further demonstrated that the axial ligand coordination significantly enhanced the adsorption and activation of CO<sub>2</sub> molecules at the Zr metal center, lowered the energy barrier for the formation of the key intermediate \*COOH, and thereby accelerated the subsequent conversion to CO. As a result, Zr-TPP-OA and Zr-TPP-PTA exhibited enhanced photocatalytic CO<sub>2</sub>-to-CO conversion efficiencies, achieving average yields of 323.1 and 336.5 μmol g<sup>-1</sup> h<sup>-1</sup>, respectively, with corresponding selectivities of 91.0 and 91.3%, surpassing most recently reported photocatalysts. This work proposes a molecular-level perspective for the design and synthesis of advanced porphyrin-based photocatalysts by leveraging axial ligand engineering to simultaneously enhance optoelectronic properties and efficient surface reactions for CO<sub>2</sub> reduction.

## 2. RESULTS AND DISCUSSION

We report a facile hydrothermal strategy to synthesize zirconium (Zr) porphyrin coordination compounds featuring axial ligands, as illustrated in Scheme 1. First, Zr-TPP was synthesized by coordinating Zr (IV) metal centers with meso-tetraphenyl porphyrin (TPP) molecules. Subsequently, oxalic acid (OA) and p-phthalic acid (PTA) were introduced as axial ligands to integrate with the metal center to obtain Zr (IV) meso-tetraphenyl porphyrin-oxalic acid (Zr-TPP-OA) and Zr (IV) meso-tetraphenyl porphyrin-p-phthalic acid (Zr-TPP-PTA). Details can be seen in the Experimental Section of the Supporting Information, and the optimized geometries are shown in Figure S2.

**2.1. Characterization of the Morphology and Structure.** The SEM images of these Zr-TPP-based coordination complexes are shown in Figure 1a–c. As-prepared Zr-TPP, Zr-TPP-OA, and Zr-TPP-PTA all exhibit irregular particle morphologies and stochastic size distributions. In addition, energy-dispersive X-ray spectroscopy (EDS) was carried out for semiquantitative composition analysis. As shown in Figure S3, the Zr:Cl atomic ratio (1.37:2.81) of pristine Zr-TPP aligned well with the theoretical value of 1:2. After the introduction of axial ligands, the atomic ratios of Zr-TPP-OA (1.03:0.36) and Zr-TPP-PTA (1.25:0.16) increased dramatically, which strongly proved that the axial ligand formed a new Zr–O coordination by replacing the Cl at the fifth and sixth coordination sites. Powder X-ray diffraction (XRD) and Fourier transform infrared (FTIR) spectroscopy were first conducted to analyze the structural information on all samples. As shown in Figure 1d, the XRD patterns of all Zr-based porphyrins displayed similar characteristic peaks, indicating that the introduction of axial ligands did not significantly alter the crystalline structure of the porphyrins. Notably, Zr-TPP-OA and Zr-TPP-PTA demonstrated a remarkably sharper peak at 7.2° compared to that of Zr-TPP, suggesting an enhanced interlayer stacking order.<sup>19</sup> This structural optimization might facilitate the diffusion of the CO<sub>2</sub> molecules to the active sites. The FTIR spectra of all samples (Figure 1e) exhibited characteristic vibration modes at 655 cm<sup>-1</sup> and the region of 1000–1600 cm<sup>-1</sup>, corresponding to the Zr–N stretching vibrations and the porphyrin ring in-plane deformation modes, respectively.<sup>20,21</sup> The distinctive C=N stretching vibration of the porphyrin appears at 1620 cm<sup>-1</sup>.<sup>22</sup> Compared to pristine Zr-TPP, Zr-TPP-OA and Zr-TPP-PTA displayed two additional vibration modes at 460 and 1687 cm<sup>-1</sup>, which could be assigned to the Zr–O stretching vibrations and the asymmetric stretching of carboxylate groups (–COO<sup>-</sup>), respectively, suggesting the successful incorporation of axial ligands through Zr–O coordination with the metalloporphyrin centers.<sup>23,24</sup>

Furthermore, to verify the chemical states of the individual elements in the as-prepared catalysts, X-ray photoelectron spectroscopy (XPS) was performed. As shown in Figure 1f, the full XPS spectra show the signals at 185.5, 284.5, 400.1, and 532.5 eV for Zr 3d, C 1s, N 1s, and O 1s in Zr-TPP-OA and Zr-TPP-PTA. In Zr-TPP, the signal of Cl 2p appears at 200 eV, whereas it is significantly weakened in Zr-TPP-OA and Zr-TPP-PTA, demonstrating the introduction of OA and PTA and their substitution for Cl atoms. The chemical states and coordination environment of Zr species in the Zr-TPP-based

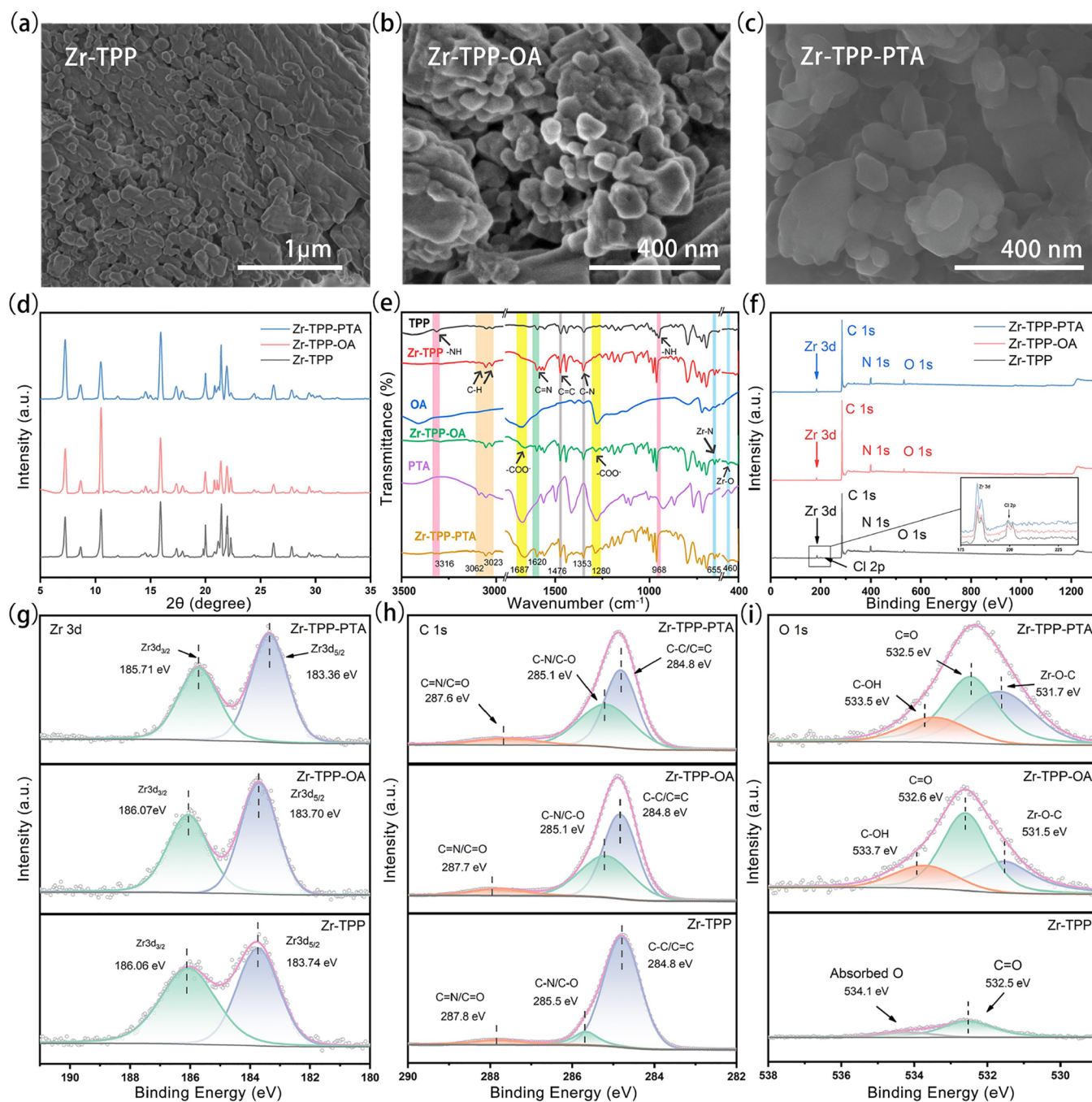


**Figure 1.** SEM images of (a) Zr-TPP, (b) Zr-TPP-OA, and (c) Zr-TPP-PTA. (d) XRD patterns of Zr-TPP, Zr-TPP-OA, and Zr-TPP-PTA. (e) FTIR spectra of TPP, OA, PTA, Zr-TPP, Zr-TPP-OA, and Zr-TPP-PTA in the range of 3500–400  $\text{cm}^{-1}$ . Survey spectrum (f) and high-resolution (g) Zr 3d, (h) C 1s, and (i) O 1s XPS spectra of Zr-TPP, Zr-TPP-OA, and Zr-TPP-PTA.

coordination compounds were investigated by using high-resolution Zr 3d XPS spectra. As shown in Figure 1g, the high-resolution Zr 3d spectra in Zr-TPP exhibit two peaks of Zr 3d<sub>5/2</sub> and Zr 3d<sub>3/2</sub> at 183.74 and 186.06 eV. The peaks of Zr in Zr-TPP-PTA shift about 0.35 eV, and in Zr-TPP-OA, they shift about 0.04 eV toward the lower binding energy, indicating an increase in electron density surrounding the Zr atoms with the introduction of axial ligands.<sup>25</sup> The XPS spectrum of C 1s in Figure 1h indicates the existence of bonds C–C/C=C at 284.8 eV, C–N/C–O at 285.1 eV, and C=N/C=O at 287.6 eV.<sup>26,27</sup> In addition, the peaks at 291.7 eV for Zr-TPP-PTA and 292.1 eV for Zr-TPP-OA may be attributed to –COOH

groups. Moreover, the XPS spectrum of O 1s in Figure 1i has three distinct peaks in Zr-TPP-OA and Zr-TPP-PTA at 531.7, 532.5, and 533.5 eV, corresponding to Zr–O–C, C=O, and C–OH, respectively.<sup>25,28</sup> This indicates the coordination of carboxylate oxygen in the added axial ligands with the metal center Zr. The O 1s spectrum of Zr-TPP has two peaks, which can be attributed to C=O in *N,N*-dimethylformamide used during the synthesis process and surface adsorbed O. Also, the N 1s spectrum (Figure S4) shows a similar chemical type of N in the three catalysts, where the three peaks are observed at around 397.9, 400.1, and 403.1 eV and can be defined as pyridinic N, pyrrolic-N, and oxidized N, respectively.<sup>29,30</sup> The

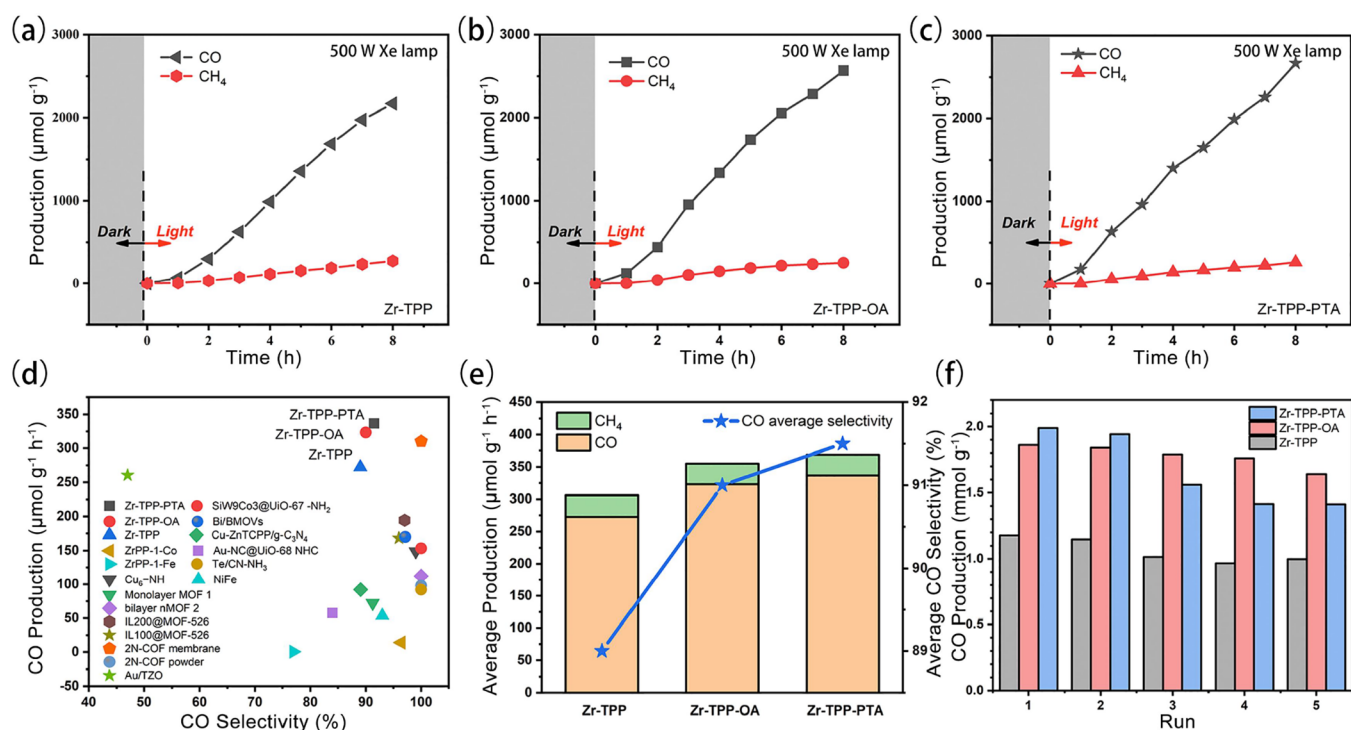


**Figure 2.** Time-dependent CO and CH<sub>4</sub> production upon xenon lamp irradiation for (a) Zr-TPP, (b) Zr-TPP-OA, and (c) Zr-TPP-PTA. (d) Performance comparison with reported representative photocatalysts. (e) Production rates and selectivity of Zr-TPP-OA/PTA over 8 h. (f) Durability measurements.

Brunauer–Emmett–Teller (BET) surface area (Figure S5) of the samples was conducted under N<sub>2</sub> adsorption at 77 K. The overall adsorption capacity of the samples is very small. Zr-TPP-PTA exhibited the largest BET surface area (26.7 m<sup>2</sup> g<sup>-1</sup>) and the optimal photoreduction CO<sub>2</sub> performance.

## 2.2. Catalytic Performance for CO<sub>2</sub> Photoreduction.

The photocatalytic performance for CO<sub>2</sub> reduction of all as-prepared photocatalysts was evaluated in a CO<sub>2</sub>-saturated solution under xenon lamp irradiation. As shown in Figure 2a–c, in a dark environment, using Zr-TPP as a catalyst, no other gases were produced in the reaction system. However, under xenon lamp illumination, the amount of generated CO rapidly increased over time, exhibiting a near-linear correlation with time. Alongside CO, a small quantity of CH<sub>4</sub> was also detected in the illuminated catalytic system. After 8 h of illumination, the amounts of CO and CH<sub>4</sub> were 2179.5 and 269.1 μmol g<sup>-1</sup>, respectively. The average production rates for CO and CH<sub>4</sub> were 272.43 and 33.6 μmol g<sup>-1</sup> h<sup>-1</sup> for Zr-TPP, respectively. Notably, the selectivity of CO formation was 89.0%. When tested under similar conditions, Zr-TPP-OA and Zr-TPP-PTA exhibited improved CO production capabilities. As shown in Figure 2b, after 8 h of illumination, using Zr-TPP-OA as a photocatalyst, 2565.5 μmol g<sup>-1</sup> CO and 255.2 μmol g<sup>-1</sup> CH<sub>4</sub> were produced. The average yields were 323.1 μmol g<sup>-1</sup> h<sup>-1</sup> for CO and 31.9 μmol g<sup>-1</sup> h<sup>-1</sup> for CH<sub>4</sub>. Similarly, Figure 2c indicates that after 8 h of illumination, Zr-TPP-PTA produced 2692.4 μmol g<sup>-1</sup> CO and 256.8 μmol g<sup>-1</sup> CH<sub>4</sub>, resulting in average yields of 336.5 μmol g<sup>-1</sup> h<sup>-1</sup> for CO and 32.1 μmol g<sup>-1</sup> h<sup>-1</sup> for CH<sub>4</sub>. Notably, the CO production rate of Zr-TPP-PTA was higher than that of Zr-TPP-OA in this study and surpassed other porphyrin-based MOFs or other classes of materials reported previously<sup>31–42</sup> (Figure 2d and Table S1). Figure 2e presents a comparative analysis of the average production rates of CO and CH<sub>4</sub> across these complexes. The results

demonstrate that the photocatalytic CO production of Zr-TPP-PTA is the highest of the as-prepared catalysts, which shows that the axial ligands have increased the photocatalytic performance. Also, Zr-TPP-OA and Zr-TPP-PTA exhibited high selectivities of 91.0 and 91.5% for CO production, indicating a preferential generation of CO. Then, control experiments were conducted to validate that the reduction of CO<sub>2</sub> relies only on these catalysts (Figure S6 and Table S2). In the absence of the photocatalyst and hole giver TEOA, barely CO and CH<sub>4</sub> were formed. Additionally, when CO<sub>2</sub> was substituted with Ar, no CO or CH<sub>4</sub> products were detected, confirming that all of the carbon-containing products originated from CO<sub>2</sub>.

The recyclability of photocatalysts is crucial for evaluating their performance. To assess this, we conducted repeat experiments using the as-prepared photocatalysts. After 6 h of illumination, the catalyst powders were collected and subjected to identical conditions for reuse. As depicted in Figure 2f, five consecutive cycles were performed. The CO production of Zr-TPP and Zr-TPP-OA remained relatively stable, whereas Zr-TPP-PTA showed a slight decrease in the level of CO generation starting from the third cycle. The structure of the catalysts after the CO<sub>2</sub> reduction reaction was further investigated by XRD (Figure S7). The XRD patterns of recycled catalysts confirm that their crystal phase structure remains unchanged but shows a slight broadening of the diffraction peaks. We presume that Zr-TPP and Zr-TPP-OA have better structural stability. However, Zr-TPP-PTA may undergo slight decomposition during the reaction, altering its structure and consequently affecting its catalytic activity. Therefore, we have verified that the introduction of axial ligands for metalloporphyrins is a method to improve the performance of photocatalytic CO production, but the stability may be reduced after the modification.

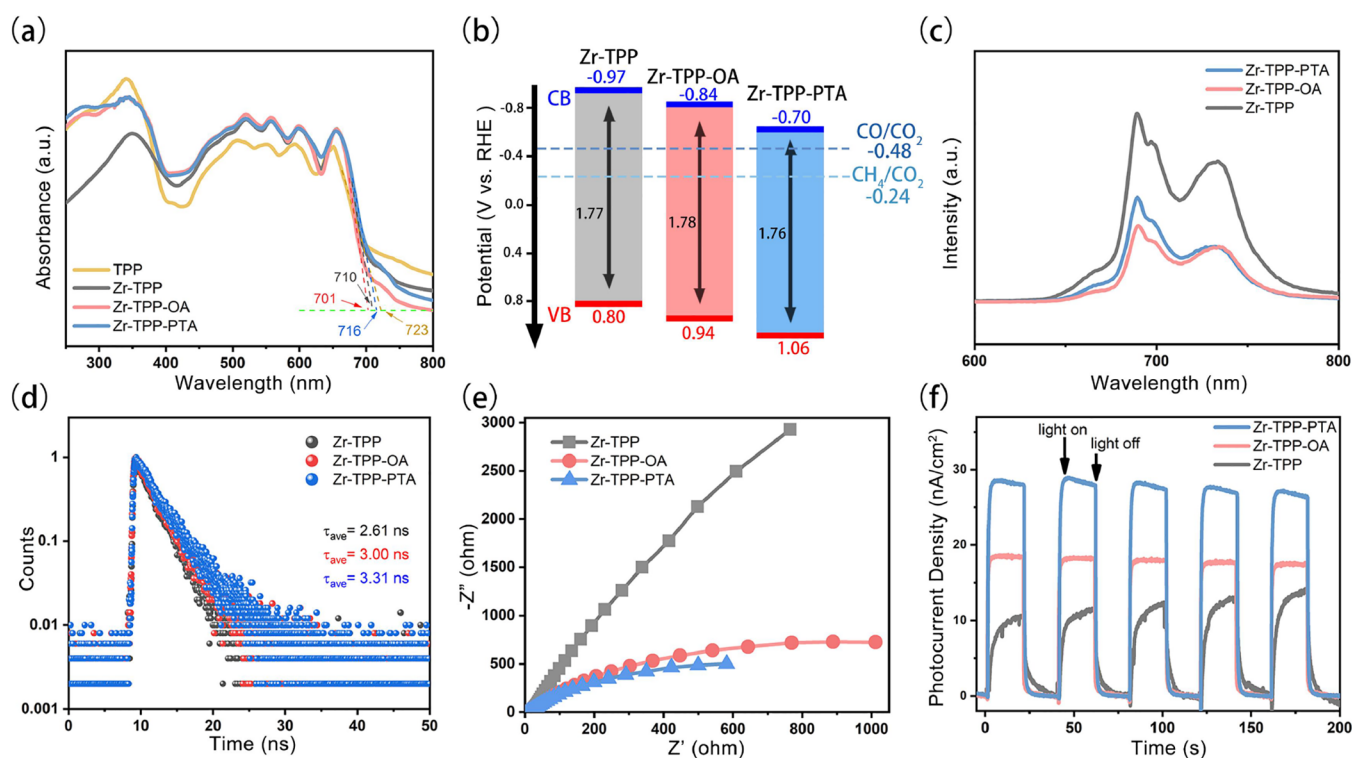


**Figure 3.** (a) UV/vis diffuse reflectance spectra (UV-vis DRS) of Zr-TPP, Zr-TPP-OA, and Zr-TPP-PTA. (b) Schematic diagram of the band structure of Zr-TPP, Zr-TPP-OA, and Zr-TPP-PTA. (c) PL spectra, (d) TRPL spectra, (e) EIS, and (f) TPR spectra of Zr-TPP, Zr-TPP-OA, and Zr-TPP-PTA.

**2.3. Light Absorption and Carrier Separation.** The optical properties and band structures of Zr-based porphyrins were systematically investigated by UV-visible diffuse reflectance spectroscopy (UV-vis DRS) and Mott-Schottky measurements. As shown in Figure 3a, all samples exhibited a broad spectral absorption range, with a characteristic Soret band centered at 350 nm originating from the conjugated  $\pi \rightarrow \pi^*$  electronic transition of the porphyrin derivatives. Notably, the absorption peak intensity of Zr-TPP-OA and Zr-TPP-PTA was significantly improved after the introduction of axial ligands, which could be attributed to the optimized charge migration between metal centers and functionalized axial ligands.<sup>24</sup> Based on the Tauc plots obtained from the transformed Kubelka-Munk function, the band gaps ( $E_g$ ) of Zr-TPP, Zr-TPP-OA, and Zr-TPP-PTA were calculated to be 1.77, 1.78, and 1.76 eV, respectively (Figure S8). As revealed by Mott-Schottky plots, all samples showed typical n-type semiconductor characteristics, and the flat band potentials of Zr-TPP-OA ( $-0.74$  V vs RHE) and Zr-TPP-PTA ( $-0.60$  V vs RHE) were slightly higher than that of Zr-TPP ( $-0.87$  V vs RHE)<sup>43,44</sup> (Figure S9). Based on the above results, the band structures of three metalloporphyrins are outlined in Figure 3b. Notably, the conduction band minimums (CBMs) of all samples are negative enough compared to the reduction potentials of CO/CO<sub>2</sub> ( $-0.48$  V vs RHE) and CH<sub>4</sub>/CO<sub>2</sub> ( $-0.24$  V vs RHE), indicating the thermodynamic feasibility of CO<sub>2</sub> photoreduction. However, both CBM and valence band maximum positions of Zr-TPP-OA and Zr-TPP-PTA were much lower than those of Zr-TPP, reflecting the effective regulation of the electronic structure of metalloporphyrins by axial ligands.

Photoluminescence (PL) and time-resolved photoluminescence (TRPL) spectroscopy were first performed to elucidate

the role of axial ligands in enhancing the separation efficiency of photogenerated carriers. As illustrated in Figure 3c, the fluorescence intensity of Zr-TPP-OA and Zr-TPP-PTA was markedly lower than that of Zr-TPP, indicating the suppressed recombination of photogenerated electron-hole pairs. Meanwhile, TRPL spectra were recorded and fitted with a biexponential decay function (Figure S3) and Table S3). The average lifetimes of photogenerated carriers ( $\tau_{\text{avg}}$ ) of Zr-TPP, Zr-TPP-OA, and Zr-TPP-PTA were calculated to be 2.61, 3.00, and 3.31 ns, respectively. The prolonged  $\tau_{\text{avg}}$  decay after the introduction of the axial ligand indicates improved separation efficiency of photogenerated carriers. Electrochemical impedance spectroscopy (EIS) and transient photocurrent response (TPR) tests were further carried out to explore the photogenerated carrier transfer efficiency. As shown in Figure 3e, Zr-TPP-OA and Zr-TPP-PTA possess smaller Nyquist plot radii than Zr-TPP, indicating a relatively lower interface charge transfer resistance ( $R_{\text{ct}}$ ).<sup>37</sup> Besides, Zr-TPP-OA and Zr-TPP-PTA exhibited much enhanced TPR intensity under visible-light irradiation (Figure 3f). Therefore, the introduction of axial ligands in Zr-TPP can remarkably enhance the efficiency of photogenerated carrier separation and transport, facilitating the achievement of effective photocatalytic reactions.

To gain deeper insights into the charge interactions between the axial ligands and the metal center, charge density difference of all samples was calculated based on density functional theory (DFT).<sup>45</sup> It is worth noting that the yellow and cyan regions correspond to charge accumulation and depletion, respectively, reflecting electronic redistribution upon ligand coordination. As shown in Figure S10, the Zr metal center exhibits pronounced electron accumulation after axial ligand coordination, suggesting substantial electron transfer from the

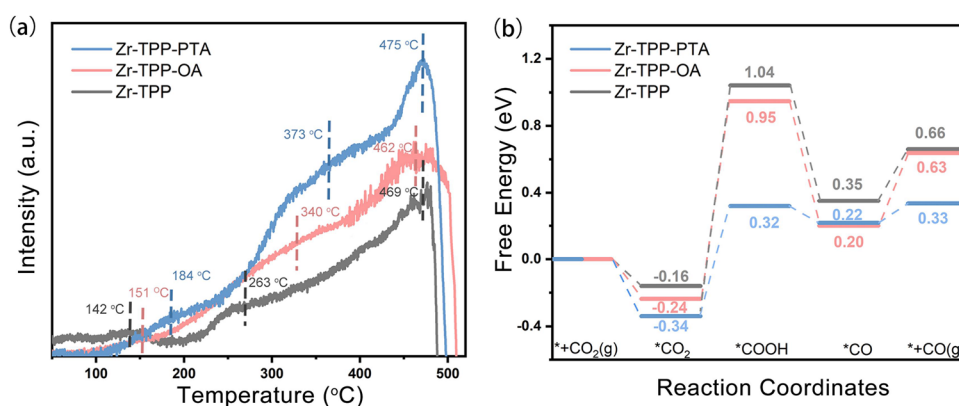


**Figure 4.** (a) CO<sub>2</sub>-TPD of Zr-TPP, Zr-TPP-OA, and Zr-TPP-PTA. (b) Free energy diagram of the photocatalytic reduction of CO<sub>2</sub> to CO over Zr-TPP, Zr-TPP-OA, and Zr-TPP-PTA.

axial ligands to the metal center, which was also consistent with the XPS results, further corroborating the ligand-induced modulation of the electronic environment. The results indicate that the optimized electronic structure promotes the efficient separation of photogenerated carriers. Meanwhile, the electron-rich metal center facilitates the subsequent activation and photoreduction of CO<sub>2</sub> molecules, underscoring the pivotal role of axial ligands in improving the overall photocatalytic performance of the Zr-TPP.

**2.4. Mechanism of Photocatalytic CO<sub>2</sub> Reduction.** A combination of experimental investigations and theoretical calculations was employed to further elucidate the role of axial ligands in enhancing the photocatalytic CO<sub>2</sub> reduction performance. First, CO<sub>2</sub> temperature-programmed desorption (CO<sub>2</sub>-TPD) tests were conducted to evaluate the CO<sub>2</sub> adsorption capacity of the as-prepared photocatalysts. As shown in Figure 4a, all samples exhibited weak physical adsorption below 200 °C.<sup>46</sup> However, Zr-TPP-OA and Zr-TPP-PTA showed significantly stronger chemical desorption signals compared to Zr-TPP in the temperature range of 250–500 °C, indicating enhanced CO<sub>2</sub> adsorption and increased reaction affinity.

Deeper insights into the mechanism of CO<sub>2</sub> adsorption and activation were further investigated via DFT calculations. Figure S11 and Table S4 show the optimized CO<sub>2</sub> adsorption configurations and corresponding CO<sub>2</sub> adsorption energy ( $\Delta E_{\text{ads}}$ ) of all photocatalysts. The results revealed that the CO<sub>2</sub> molecule was more favorably adsorbed onto the Zr metal centers, indicating that Zr could serve as the CO<sub>2</sub> adsorption and activation site during the photocatalytic CO<sub>2</sub> reduction reaction (Figure S11). Notably, Zr-TPP-OA and Zr-TPP-PTA exhibited more negative  $\Delta E_{\text{ads}}$  values and decreased the O=C=O bond angles compared to Zr-TPP (Table S4), suggesting that axial ligands significantly enhanced the binding affinity to the CO<sub>2</sub> molecule of the metal center while promoting the activation of the adsorbed CO<sub>2</sub> molecules.

Particularly, the formation of the key intermediate \*COOH was commonly recognized as the rate-limiting step.<sup>47,48</sup> Therefore, the free energy changes of the elementary CO<sub>2</sub> reduction reaction steps were calculated. As depicted in Figure 4b, Zr-TPP-OA and Zr-TPP-PTA exhibited lower \*COOH formation energy barriers, thus promoting the conversion to CO. These results fully confirmed that the introduction of axial ligands enhanced the intrinsic activity of the Zr-TPP system for photocatalytic CO<sub>2</sub>-to-CO conversion through strong coordination interactions with the metal center.

### 3. CONCLUSIONS

To sum up, we successfully developed a series of metal-porphyrin-based photocatalysts functionalized with axial ligands through a facile hydrothermal synthesis method. These well-designed axial coordination complexes exhibit evidently improved photocatalytic performance, achieving over 90% selectivity for CO<sub>2</sub>-to-CO conversion under irradiation. Comprehensive experiments and theoretical calculations reveal that the axial ligands regulate the local electronic structure of the metal center through coordination interactions, thereby promoting efficient separation and transport of photogenerated carriers. Furthermore, axial ligands promote the adsorption and activation of CO<sub>2</sub> molecules at metal active sites, reduce the activation energy required for the generation of the key intermediate \*COOH, and accelerate its subsequent reduction to CO. Our work provides valuable molecular-level insights into the strategic design of efficient photocatalysts and contributes to a deeper understanding of the catalytic mechanisms for sustainable energy applications.

### ■ ASSOCIATED CONTENT

#### Supporting Information

The Supporting Information is available free of charge at <https://pubs.acs.org/doi/10.1021/acsaem.4c03295>.

Experimental Section, chemicals, synthesis process, and measurements; Figure S1, diagram of the photocatalytic reactor; Figure S2, simulated unit structure of the samples; Figure S3, EDS spectroscopy of the samples; Figure S4, high-resolution N 1s XPS spectra of the samples; Figure S5, N<sub>2</sub> adsorption and desorption isotherms of the samples; Figure S6, photocatalytic CO<sub>2</sub> reduction control experiments; Figure S7, PXRD patterns of the samples before and after the CO<sub>2</sub> reduction reaction; Figure S8, estimated band gaps of the samples by Tauc plots; Figure S9, Mott–Schottky plot of the samples; Figure S10, optimized molecular structure model and corresponding charge density difference of the samples; Figure S11, optimized CO<sub>2</sub> adsorption configurations on the samples; Table S1, comparison of the photocatalytic CO<sub>2</sub> reduction activities of recently reported catalysts; Table S2, photocatalytic CO<sub>2</sub> reduction control experiment; Table S3, fitting results of TRPL acquired from the

samples; and Table S4, details of CO<sub>2</sub> adsorption on the samples (PDF)

## AUTHOR INFORMATION

### Corresponding Author

**Jing Sun** – State Key Lab of High Performance Ceramics and Superfine Microstructure, Shanghai Institute of Ceramics, Chinese Academy of Sciences, Shanghai 201899, China; [orcid.org/0000-0003-1101-1584](https://orcid.org/0000-0003-1101-1584); Email: [jingsun@mail.sic.ac.cn](mailto:jingsun@mail.sic.ac.cn)

### Authors

**Chenyue Yong** – State Key Lab of High Performance Ceramics and Superfine Microstructure, Shanghai Institute of Ceramics, Chinese Academy of Sciences, Shanghai 201899, China; University of Chinese Academy of Sciences, Beijing 100049, China; [orcid.org/0009-0006-1610-9299](https://orcid.org/0009-0006-1610-9299)

**Chi Song** – State Key Lab of High Performance Ceramics and Superfine Microstructure, Shanghai Institute of Ceramics, Chinese Academy of Sciences, Shanghai 201899, China

**Guanhong Lu** – State Key Lab of High Performance Ceramics and Superfine Microstructure, Shanghai Institute of Ceramics, Chinese Academy of Sciences, Shanghai 201899, China

**Xiao Wang** – State Key Lab of High Performance Ceramics and Superfine Microstructure, Shanghai Institute of Ceramics, Chinese Academy of Sciences, Shanghai 201899, China; [orcid.org/0000-0001-9786-8153](https://orcid.org/0000-0001-9786-8153)

**Guanqing Song** – State Key Lab of High Performance Ceramics and Superfine Microstructure, Shanghai Institute of Ceramics, Chinese Academy of Sciences, Shanghai 201899, China; University of Chinese Academy of Sciences, Beijing 100049, China

**Gansheng Shi** – State Key Lab of High Performance Ceramics and Superfine Microstructure, Shanghai Institute of Ceramics, Chinese Academy of Sciences, Shanghai 201899, China

**Yan Wang** – State Key Lab of High Performance Ceramics and Superfine Microstructure, Shanghai Institute of Ceramics, Chinese Academy of Sciences, Shanghai 201899, China; [orcid.org/0000-0002-0971-5032](https://orcid.org/0000-0002-0971-5032)

**Xiaofeng Xie** – State Key Lab of High Performance Ceramics and Superfine Microstructure, Shanghai Institute of Ceramics, Chinese Academy of Sciences, Shanghai 201899, China; [orcid.org/0000-0003-1789-1084](https://orcid.org/0000-0003-1789-1084)

Complete contact information is available at: <https://pubs.acs.org/10.1021/acsaem.4c03295>

### Author Contributions

C.Y. was responsible for executing the experiments, preparing the samples, evaluating the properties, and drafting the manuscript. G.L., C.S., G.S., G.S., Y.W., X.X., and J.S. provided valuable comments and revised the manuscript. J.S. supervised this project. All authors have concurred and approved the definitive version of this manuscript.

### Notes

The authors declare no competing financial interest.

## ACKNOWLEDGMENTS

This work was financially supported by the Shanghai Commission of Science and Technology Program (CXXT-2023-01) and the National Natural Science Foundation of China (52072387).

## REFERENCES

- (1) Byrne, B.; Liu, J. J.; Bowman, K. W.; Pascolini-Campbell, M.; Chatterjee, A.; Pandey, S.; Miyazaki, K.; van der Werf, G. R.; Wunch, D.; Wennberg, P. O.; Roehl, C. M.; Sinha, S. Carbon emissions from the 2023 Canadian wildfires. *Nature* **2024**, *633*, 835–839.
- (2) He, H. Z.; Kramer, R. J.; Soden, B. J.; Jeevanjee, N. State dependence of CO<sub>2</sub> forcing and its implications for climate sensitivity. *Science* **2023**, *382* (6674), 1051–1056.
- (3) Zhang, W. X.; Zhou, T. J.; Wu, P. L. Anthropogenic amplification of precipitation variability over the past century. *Science* **2024**, *385* (6707), 427–432.
- (4) Ding, X.; Liu, W. X.; Zhao, J. H.; Wang, L.; Zou, Z. G. Photothermal CO<sub>2</sub> catalysis toward the synthesis of solar fuel: from material and reactor engineering to techno-economic analysis. *Adv. Mater.* **2025**, *37*, No. 2312093.
- (5) Kosugi, K.; Akatsuka, C.; Iwami, H.; Kondo, M.; Masaoka, S. Iron-complex-based supramolecular framework catalyst for visible-light-driven CO<sub>2</sub> reduction. *J. Am. Chem. Soc.* **2023**, *145* (19), 10451–10457.
- (6) Rao, H.; Chmidt, L. C. S.; Bonin, J.; Robert, M. Visible-light-driven methane formation from CO<sub>2</sub> with a molecular iron catalyst. *Nature* **2017**, *548* (7665), 7674.
- (7) Cao, X. Y.; Zhao, L. L.; Wulan, B. R.; Tan, D. X.; Chen, Q. W.; Ma, J. Z.; Zhang, J. T. Atomic bridging structure of nickel-nitrogen-carbon for highly efficient electrocatalytic reduction of CO<sub>2</sub>. *Angew. Chem., Int. Ed.* **2022**, *61* (6), No. e202113918.
- (8) Li, D.; Wang, K.; Li, J.; Li, Z.; Wang, H.; Wang, Y. Strategies for optimizing the efficiency and selectivity of photocatalytic aqueous CO<sub>2</sub> reduction: Catalyst design and operating conditions. *Nano Energy* **2025**, *133*, No. 110460.
- (9) Ding, J. H.; Guan, X. Y.; Lv, J.; Chen, X. H.; Zhang, Y.; Li, H.; Zhang, D. L.; Qiu, S. L.; Jiang, H. L.; Fang, Q. R. Three-dimensional covalent organic frameworks with Ultra-Large Pores for Highly Efficient Photocatalysis. *J. Am. Chem. Soc.* **2023**, *145* (5), 3248–3254.
- (10) Tian, X. M.; Lin, C. S.; Zhong, Z.; Li, X. X.; Xu, X.; Liu, J. J.; Kang, L. T.; Chai, G. L.; Yao, J. N. Effect of axial coordination of iron porphyrin on their nanostructures and photocatalytic performance. *Cryst. Growth Des.* **2019**, *19* (6), 3279–3287.
- (11) Abdinejad, M.; Tang, K.; Dao, C.; Saedy, S.; Burdyny, T. Immobilization strategies for porphyrin-based molecular catalysts for the electroreduction of CO<sub>2</sub>. *J. Mater. Chem. A* **2022**, *10* (14), 7626–7636. [10.1039/D2TA00876A](https://doi.org/10.1039/D2TA00876A)
- (12) Carrillo-Carrion, C.; Farrando-Perez, J.; Daemen, L. L.; Cheng, Y. Q.; Ramirez-Cuesta, A. J.; Silvestre-Albero, J. Zr-Porphyrin Metal–Organic Framework as nanoreactor for boosting the formation of hydrogen clathrates. *Angew. Chem., Int. Ed.* **2024**, *63* (6), No. e202315280.
- (13) Wang, J.; Dou, S.; Wang, X. Structural tuning of heterogeneous molecular catalysts for electrochemical energy conversion. *Sci. Adv.* **2021**, *7* (13), No. eabf3989.
- (14) Pizarro, A.; Abarca, G.; Gutiérrez-Cerón, C.; Cortés-Arriagada, D.; Bernardi, F.; Berrios, C.; Silva, J. F.; Rezende, M. C.; Zagal, J. H.; Oñate, R.; Ponce, I. Building pyridinium molecular wires as axial ligands for tuning the electrocatalytic activity of iron phthalocyanines for the oxygen reduction reaction. *ACS Catal.* **2018**, *8* (9), 8406–8419.
- (15) Qian, C.; Chen, D.; Zhao, H. Axially coordinated oligomer of ferrocene-based porphyrin with fullerene C60 for spectroscopic and photocurrent studies. *Synth. Met.* **2021**, *271*, No. 116635.
- (16) Zheng, J.; Zhou, D.; Han, J.; Liu, J.; Cao, R.; Lei, H.; Bian, H.; Fang, Y. Non-negligible axial ligand effect on electrocatalytic CO<sub>2</sub> reduction with iron porphyrin complexes. *J. Phys. Chem. Lett.* **2022**, *13* (50), 11811–11817.
- (17) Li, X.; Li, P.; Yang, J.; Xie, L.; Wang, N.; Lei, H.; Zhang, C.; Zhang, W.; Lee, Y.-M.; Zhang, W.; Fukuzumi, S.; Nam, W.; Cao, R. A cobalt(II) porphyrin with a tethered imidazole for efficient oxygen reduction and evolution electrocatalysis. *J. Energy. Chem.* **2023**, *76*, 617–621.

- (18) Xue, H.-Z.; Wu, J.-H.; Wang, B.-W.; Gao, S.; Zhang, J.-L. Coordination induced spin state transition switches the reactivity of nickel (II) porphyrin in hydrogen evolution reaction. *Angew. Chem., Int. Ed.* **2025**, *64* (1), No. e202413042.
- (19) Li, X. H.; Zhang, Y. Z.; Wang, W. X.; Meng, J. J.; Li, K.; Lin, W. X.; Peng, Z. Q.; Wan, J. M.; Hu, Z. W. Fabrication of 1D long chain-like metal porphyrin-based coordination complexes for high-efficiency hydrogen evolution and photoelectric response. *Int. J. Hydrogen Energy* **2019**, *44* (33), 18072–18082.
- (20) Liu, Y.; Guo, L.; Chen, Y.; Wang, Y.; Xu, G.; Gu, L.; Yu, Z.; Yuan, Y. A porphyrin-based metal-organic framework Al-TCPP for highly selective sensing of copper ions with exceptional low limit of detection. *J. Environ. Chem. Eng.* **2023**, *11* (5), No. 111021.
- (21) Anjali, K.; Aswini, M. S.; Aswin, P.; Ganesh, V.; Sakthivel, A. Iridium tetra(4-carboxyphenyl) porphyrin, calix pyrrole and tetraphenyl porphyrin complexes as potential hydrogenation catalysts. *Eur. J. Inorg. Chem.* **2019**, *2019* (38), 4087–4094.
- (22) Zhen, W.; Kang, D. W.; Fan, Y.; Wang, Z.; Germanas, T.; Nash, G. T.; Shen, Q.; Leech, R.; Li, J.; Engel, G. S.; Weichselbaum, R. R.; Lin, W. Simultaneous protonation and metalation of a porphyrin covalent organic framework enhance photodynamic therapy. *J. Am. Chem. Soc.* **2024**, *146* (24), 16609–16618.
- (23) Su, Q.; Li, J.; Wang, B.; Li, Y.; Hou, L. A Direct Z-scheme Bi<sub>2</sub>MoO<sub>6</sub>/UiO-66-NH<sub>2</sub> heterojunctions for enhanced photocatalytic degradation of ofloxacin and ciprofloxacin under visible light. *Appl. Catal., B* **2022**, *318*, No. 121820.
- (24) Pi, X.; Wang, Y.; Kan, X. A self-enhanced electrochemiluminescence aptasensor Zr-porphyrin modified with polyamidoamine for sensitive detection of lincomycin. *Food Chem.* **2025**, *464*, No. 141846.
- (25) Wang, W.; Song, S.; Wang, P.; He, M.; Fang, Z.; Yuan, X.; Li, H.; Li, C.; Wang, X.; Wei, Y.; Song, W.; Xu, H.; Li, Z. Chemical bonding of g-C<sub>3</sub>N<sub>4</sub>/UiO-66(Zr/Ce) from Zr and Ce single atoms for efficient photocatalytic reduction of CO<sub>2</sub> under visible light. *ACS Catal.* **2023**, *13* (7), 4597–4610.
- (26) Wu, F. S.; Su, H. F.; Wang, K.; Wong, W. K.; Zhu, X. J. Facile synthesis of N-rich carbon quantum dots from porphyrins as efficient probes for bioimaging and biosensing in living cells. *Int. J. Nanomedicine* **2017**, *12*, 7375–7391.
- (27) Zhang, X.; Liu, Y.; Shen, P.; Ren, L.; Han, D.; Feng, M.; Wang, H.-G. Engineering an artificial coating layer of metal porphyrin-based porous organic polymers toward high stable aqueous zinc-ion batteries. *Adv. Funct. Mater.* **2024**, *34* (33), No. 2400032.
- (28) Song, Y.; Ruan, P.; Mao, C.; Chang, Y.; Wang, L.; Dai, L.; Zhou, P.; Lu, B.; Zhou, J.; He, Z. Metal–Organic Frameworks functionalized separators for robust aqueous zinc-ion batteries. *Nano-Micro Lett.* **2022**, *14* (1), 218.
- (29) Xie, C.; Lin, L.; Huang, L.; Wang, Z.; Jiang, Z.; Zhang, Z.; Han, B. Zn-N<sub>x</sub> sites on N-doped carbon for aerobic oxidative cleavage and esterification of C(CO)-C bonds. *Nat. Commun.* **2021**, *12*, 4823.
- (30) Tan, Y.; Zhang, Z.; Chen, S.; Wu, W.; Yu, L.; Chen, R.; Guo, F.; Wang, Z.; Cheng, N. Local geometric distortion to stimulate oxygen reduction activity of atomically dispersed Zn-N<sub>x</sub> sites for Zn-air batteries. *Adv. Funct. Mater.* **2024**, *34* (10), No. 2311337.
- (31) Liang, J. X.; Yu, H.; Shi, J. J.; Li, B.; Wu, L. X.; Wang, M. Dislocated bilayer MOF enables high-selectivity photocatalytic reduction of CO<sub>2</sub> to CO. *Adv. Mater.* **2023**, *35* (10), No. e2209814.
- (32) Chen, E.-X.; Qiu, M.; Zhang, Y.-F.; Zhu, Y.-S.; Liu, L.-Y.; Sun, Y.-Y.; Bu, X.; Zhang, J.; Lin, Q. Acid and base resistant zirconium polyphenolate-metalloporphyrin scaffolds for efficient CO<sub>2</sub> photo-reduction. *Adv. Mater.* **2018**, *30* (2), No. 1704388.
- (33) Zhao, X.; Xu, Q.; Han, J.; Zhang, W.; Rao, H.; Du, D.-Y.; She, P.; Qin, J.-S. Ionic liquid modified Fe-porphyrinic Metal–Organic Frameworks as efficient and selective photocatalysts for CO<sub>2</sub> reduction. *ACS Appl. Mater. Interfaces* **2024**, *16* (20), 26272–26279.
- (34) Gao, S.; Zhang, Q.; Su, X.; Wu, X.; Zhang, X.-G.; Guo, Y.; Li, Z.; Wei, J.; Wang, H.; Zhang, S.; Wang, J. Ingenious artificial leaf based on covalent organic framework membranes for boosting CO<sub>2</sub> photoreduction. *J. Am. Chem. Soc.* **2023**, *145* (17), 9520–9529.
- (35) Dong, J.-P.; Xu, Y.; Zhang, X.-G.; Zhang, H.; Yao, L.; Wang, R.; Zang, S.-Q. Copper-sulfur-nitrogen cluster providing a local proton for efficient carbon dioxide photoreduction. *Angew. Chem., Int. Ed.* **2023**, *62* (48), No. e202313648.
- (36) Zhang, P.; Wang, T.; Ma, H.; Ma, R.; Xia, Z.; Yang, Q.; Yang, X.; Xie, G.; Chen, S. Heterointerface connection with multiple hydrogen-bonding in Z-scheme heterojunction SiW<sub>9</sub>Co<sub>3</sub>@UiO-67-NH<sub>2</sub> deciding high stability and photocatalytic CO<sub>2</sub> reduction performance. *Inorg. Chem.* **2023**, *62* (49), 20401–20411.
- (37) Liu, L.; Wang, Z.; Zhang, J.; Ruzimuradov, O.; Dai, K.; Low, J. Tunable interfacial charge transfer in a 2D–2D composite for efficient visible-light-driven CO<sub>2</sub> conversion. *Adv. Mater.* **2023**, *35* (26), No. 2300643.
- (38) Xie, S. J.; Deng, C. Y.; Huang, Q.; Zhang, C.; Chen, C. C.; Zhao, J. C.; Sheng, H. Facilitated photocatalytic CO<sub>2</sub> reduction in aerobic environment on a copper-porphyrin metal-organic framework. *Angew. Chem., Int. Ed.* **2023**, *62* (10), No. e202216717.
- (39) Huang, N.-Y.; Li, B.; Wu, D.; Chen, Z.-Y.; Shao, B.; Chen, D.; Zheng, Y.-T.; Wang, W.; Yang, C.; Gu, M.; Li, L.; Xu, Q. Crystal engineering of MOF-derived bimetallic oxide solid solution anchored with Au nanoparticles for photocatalytic CO<sub>2</sub> reduction to syngas and C<sub>2</sub> hydrocarbons. *Angew. Chem., Int. Ed.* **2024**, *63* (21), No. e202319177. (accessed 2024/12/09)
- (40) Jiang, Y.; Yu, Y.; Zhang, X.; Weinert, M.; Song, X.; Ai, J.; Han, L.; Fei, H. N-heterocyclic carbene-stabilized ultrasmall gold nano-clusters in a metal-organic framework for photocatalytic CO<sub>2</sub> reduction. *Angew. Chem., Int. Ed.* **2021**, *60* (32), 17388–17393. (accessed 2024/12/09)
- (41) Liao, H.; Huang, K.; Hou, W.; Guo, H.; Lian, C.; Zhang, J.; Liu, Z.; Wang, L. Atmosphere engineering of metal-free Te/C<sub>3</sub>N<sub>4</sub> p-n heterojunction for nearly 100% photocatalytic converting CO<sub>2</sub> to CO. *Adv. Powder Mater.* **2024**, *3* (6), No. 100243.
- (42) Xiao, Y.; Zhang, H.-T.; Zhang, M.-T. Heterobimetallic NiFe complex for photocatalytic CO<sub>2</sub> reduction: united efforts of NiFe dual sites. *J. Am. Chem. Soc.* **2024**, *146* (42), 28832–28844.
- (43) Zou, L.; Sa, R.; Zhong, H.; Lv, H.; Wang, X.; Wang, R. Photoelectron transfer mediated by the interfacial electron effects for boosting visible-light-driven CO<sub>2</sub> reduction. *ACS Catal.* **2022**, *12* (6), 3550–3557.
- (44) Xu, H.-Q.; Hu, J.; Wang, D.; Li, Z.; Zhang, Q.; Luo, Y.; Yu, S.-H.; Jiang, H.-L. Visible-Light photoreduction of CO<sub>2</sub> in a Metal–Organic Framework: boosting electron–Hole separation via electron trap states. *J. Am. Chem. Soc.* **2015**, *137* (42), 13440–13443.
- (45) Wang, T.; Zhao, N.; Shi, C.; Ma, L.; He, F.; He, C.; Li, J.; Liu, E. Interface and doping effects on Li ion storage behavior of graphene/Li<sub>2</sub>O. *J. Phys. Chem. C* **2017**, *121* (36), 19559–19567.
- (46) Wang, Z.; Zhou, W.; Wang, X.; Zhang, X.; Chen, H.; Hu, H.; Liu, L.; Ye, J.; Wang, D. Enhanced photocatalytic CO<sub>2</sub> reduction over TiO<sub>2</sub> using metalloporphyrin as the cocatalyst. *Catalysts* **2020**, *10*, 654.
- (47) Wang, Y.-R.; Huang, Q.; He, C.-T.; Chen, Y.; Liu, J.; Shen, F.-C.; Lan, Y.-Q. Oriented electron transmission in polyoxometalate-metalloporphyrin organic framework for highly selective electro-reduction of CO<sub>2</sub>. *Nat. Commun.* **2018**, *9* (1), 4466.
- (48) Fang, M.; Xu, L.; Zhang, H.; Zhu, Y.; Wong, W.-Y. Metalloporphyrin-linked mercurated graphynes for ultrastable CO<sub>2</sub> electroreduction to CO with Nearly 100% selectivity at a Current Density of 1.2 A cm<sup>-2</sup>. *J. Am. Chem. Soc.* **2022**, *144* (33), 15143–15154.